PSF modelling of the XMM Flight Mirror Modules

Y. Stockman, Y. Houbrechts, Y. Nazé, P. Rochus, J.Ph. Tock
CSL, Centre Spatial de Liège – University of Liege
B- 4031 Angleur (Liège)
Belgium
phone : 32 4 3676668, fax : 32 4 3675613, email : ystockman@ulg.ac.be.

Ph. Gondoin
ESA / ESTEC / SSD
PO BOX 299, 2200 AG Noordwijk, ZH
The Netherlands

ABSTRACT

In the frame of X-Ray Multi-Mirror Mission (XMM) testing, all the Mirror Modules have been illuminated by a vertical EUV (58.4 nm) collimated beam at the Centre Spatial de Liège (CSL). A Mirror Module consists in 58 co-focal and co-axial Wolter I mirrors. Up to now the images obtained at CSL have been used to assess the Mirror Module optical performances in a flight representative configuration, and also to verify the impact of the thermal environmental and vibration tests on the optical performance.

Due to the highly complex design of the Mirror Modules, simulating XMM images in details is very difficult. The Point Spread Function of some of the Mirror Modules presents slight asymmetry. In the facility design study, it has been demonstrated that the diffraction impact at 58.4 nm is negligible with respect to the Half Energy Width Mirror Module specification (20 to 30 arcsec on-axis). Presently all the Mirror Modules are better than 16 arcsec!

This paper presents first the diffraction contribution on the image. In a second step a Point Spread Function is built by using the metrological Mirror Shell data (SCISIM numerical model). EUV images are then analysed to evaluate the impact of the Mirror Interface Structure integration process on the Point Spread Function. An analytical model of the measured EUV PSF is developed. The modelisation technique is applied to simulate in-orbit image. Finally the different modelisations are evaluated and compared.

KEYWORDS :
X-ray optics and telescope, EUV optics, test facility, XMM, image analysis

1. INTRODUCTION

The X-ray Multi-Mirror Mission (XMM)[1] , which will be launched before 2000, is the largest space observatory built by ESA. The mission will perform spectral and imaging observation in the 0.1 to 10 keV energy range of the electromagnetic spectrum. The payload consists in 3 Mirror Assemblies (MA). Each MA contains a Mirror Module including 58 X-ray Wolter I type mirror named Mirror Shell (MS) and an X-ray baffle (XRB) to reduce straylight. Two of the three MA are equipped with a Reflection Grating Assembly (RGA) for spectral analysis.

All the MA have been tested in the Centre Spatial de Liège (CSL) facility[2]. The aim of the tests is to space qualify all the MA and to check the quality of all the optical subsystems (MM, XRB and RGA). This was performed in a dedicated facility between 96-99. These tests provided a huge quantity of images[3-4]. The paper explains how data can be used for image analysis of in-orbit images.

To help in-orbit image interpretation one approach is to use a numerical model of the MM. Such a tool has been developed by ESTEC team[5-6], and shows very good correlation to the experimental results in EUV and in X-rays. This model is also powerful in term of radiometry and image shape. However, due to the highly complex design of the MM, simulating XMM images in detail is very difficult. The measured Point Spread Function (PSF) of some MM presents slight

Paper presented at SPIEs 44th annual meeting on Optical Science, Engineering, and Instrumentation at Denver, July 1999

asymmetry due to the external cylinder integration. Implementing these effects in the numerical model is possible but increases the number of input parameters and by this way the complexity of the model.

Using the EUV images presents also drawbacks. Indeed these images are taken with a Cassegrain collimator at 58.4 nm. The collimator has an instrument profile that modifies the actual PSF of the MM. One way to recover the impact of integration PSF is to deconvolve the global PSF by the collimator instrument profile and the SCISIM model. This is a second method to help in-orbit image interpretation.

A last method proposed is to parameterise the PSF. These parameterisations could be used as initial guest on in-orbit images. A better parameterisation will then be performed on the actual in-orbit images. The parameterisation technique presents the advantage to save considerable time and computer memory.

The paper is divided as follows :

1) A description of a MM and of the test facility used to get the experimental images
2) A presentation of the MM numerical model (SCISIM), its advantages and drawbacks
3) An analysis of the experimental images and the study of deconvolution technique to take into account all the parameters degrading the MM actual PSF
4) A description of the parameterisation
5) An application to simulate in-orbit image
6) A comparison of these previous techniques in terms of image restoration.

2. XMM MM DESCRIPTION

The XMM complex design has been selected to achieve good image quality (HEW better than 16 arcsec) and high throughput. To fulfil the spectral requirements two of the three Mirror Assemblies (MA) are equipped with a Reflection Grating Assembly. The RGA consists of a main structure in Beryllium. This structure supports about 200 identical diffraction gratings which diffract the incoming beam to a common focus on the Rowland circle. Figure 1 presents the layout of the XMM MM combined with the RGA and the main characteristics of the MM and the RGA. An X-ray Baffle (XRB) is integrated 85 mm in front of the MM entrance plane. This is not represented in the layout of figure 1. The XRB is mounted to reduce straylight from sources out of the FOV (Field Of View). The baffle consists of a series of "sieve plates", made of circular strips. These plates are aligned with the MM, in such a way that they block the single hyperbola reflection without vigneting the double reflection rays. An Exit baffle (EXB) is integrated to cover the light gap between the MM and the RGA.

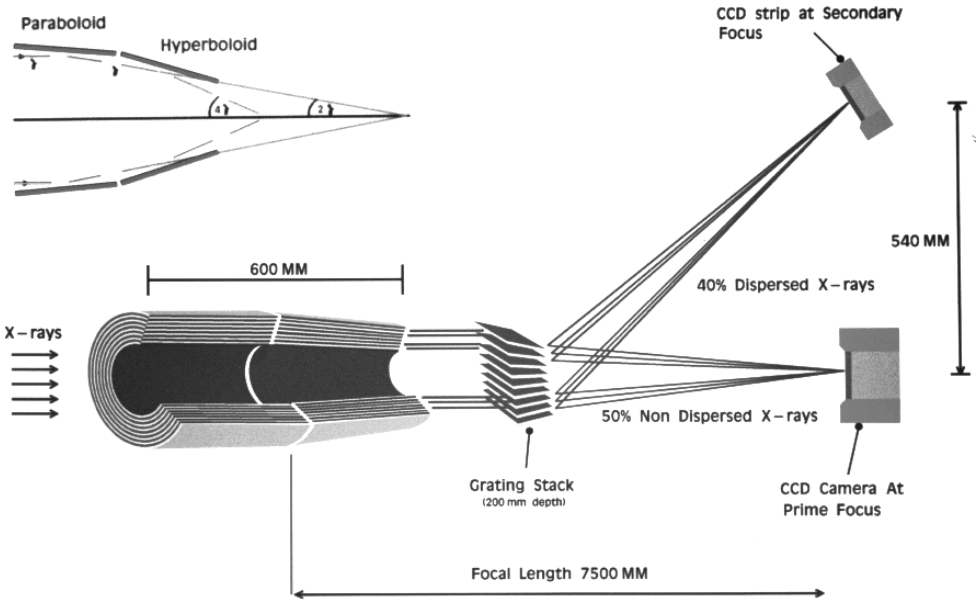

Figure 1 **: Optical layout of XMM MM combined with RGS**

Optical characteristics of a MM

Focal length : 7500 mm

HEW (0.1 – 12 keV) = 16 "
FWHM (0.1 – 12 keV) = 8 "

Diameter = 306 – 700 mm
MS thickness = 0.5 – 1 mm
Parabola length : 300 mm
Hyperbola length : 300 mm

Coating : Gold
Mirror substrate : Nickel
Number of MS : 58
MM mass = 425 kg

RGA characteristics

Number of stacks : _ 200
Stacks size : 200 x 100 mm_
Energy range : 0.1 to 3 keV
Resolving power :
250 eV at 1 keV

3. EUV AND SCISIM MODEL IMAGES

To space qualify all the MA and their optical subsystems (MM, XRB and RGA), a dedicated facility has been built at the Centre Spatial de Liège (Belgium). This facility allows a full aperture illumination in the EUV (58.4 and 30.4 nm).
An electron cyclotron resonance (ECR) source fed by He gas, emits the He I and He II lines. The source illuminates a 100 µm pinhole placed at the focal point of a Cassegrain collimator of 800 mm clear aperture. The optical axis of the collimator is aligned with respect to the local gravity. The telescope is located above the collimator and focuses the parallel beam on a back side illuminated EUV CCD detector. The CCD has 800 x 1152 pixels of 22.5 x 22.5 µm_. Thin metallic filters are put in front of the CCD detector to suppress the visible spectrum of the source.

Images[7] are available for the MM alone, the MM + XRB and the MM + XRB + RGA + EXB. FOV images are also recorded for the final flight configuration.
The images acquired with this facility are degraded by the instrumental profile of the facility. This instrumental profile includes diffraction, wavefront errors of the collimator, beam inhomogeneity and divergence of the collimator.

Because of the lack of well known cosmic X-ray sources which could serve as in-orbit calibration standard, it is necessary to perform on-ground calibration with high accuracy. Unfortunately, on-ground testing cannot be performed in fully representative operation conditions. Indeed X-ray calibration can only be performed with a finite source distance. Infinite source distance tests can only be performed in the EUV. In order to overcome these problems and to satisfy the calibration requirement, a reliable numerical model of the XMM mirror system has been developed[8]. This model uses the Mirror Shell (MS) metrology data of FM1. The model has been certified by comparing the simulated results with the experimental data[5-6]. This model is dedicated to generate calibration files.

To create the EUV facility images used hereafter, a flux of 1 photon/cm_.s during 100 s has been simulated (which is much smaller than the experimental flux) for several field angles. This provides about 180 000 rays in the focal plane. The images are then sampled by the 22.5×22.5 µm_ EUV CCD pixels size. An example is given in figure 2.

4. EUV EXPERIMENTAL IMAGES

The EUV experimental data are influenced by diffraction. During the design phase of the FOCALX facility, the trade off was to use standard device and to minimise the diffraction effects. Due to the highly nested design of XMM telescope the diffraction effects are prominent in the visible but also in the UV at 253 nm. The conclusion of the design study demonstrated that the best compromise was to use He I and if possible He II lines. The simplest way to evaluate the diffraction contribution of one MS is to use the simplified formula[10] :

$$\theta_{90} = \frac{2\lambda / D}{1-\varepsilon} \qquad [1]$$

Where θ_{90} is the angular radius containing 90 % of the spot energy, λ the wavelength, D the MS external diameter, and _ the obstruction ratio. In the case of an XMM MM, _ = 0.999015 for each MS.

From formula [1], it is obvious that with such an obstruction ratio the diffraction effect becomes quickly predominant when the wavelength increases. To take into account the total diffraction of a MM, a simple sum weighted by the MS geometrical effective area (Sn) is performed:

$$90ew(\theta) = \frac{1}{S_T}\sum_{n=1}^{58} S_n \theta_n \qquad [2]$$

Where S_T is the total geometrical effective area : $S_T = \sum_{n=1}^{58} S_n$.

This operation is exact only if the diffraction pattern between each MS is incoherent. This is the case for the actual set-up. The source coherence length (λ_/dλ) is about 1 mm, the optical path differences (OPD) between different MS varies from 0.05 to 7 mm by design. Adding the variations of the individual MS focal lengths which are different by a few mm due to the fabrication and alignment processes, it is valuable to assume this incoherent situation.
Using formula [2], gives 4.8 arcsec. To achieve a better evaluation of the Encircled Energy Function (EEF), the diffraction is computed by using the relation[11]

$$I(x,y) = \frac{I_0}{(1-\varepsilon^2)^2} \cdot \left[\left(\frac{2.J_1(ka\omega)}{ka\omega} \right) - \varepsilon^2 \left(\frac{2J_1(k\varepsilon a\omega)}{k\varepsilon a\omega} \right) \right]^2 \qquad [3]$$

with I(x,y) the intensity at the (x,y) point in the image plane, J_1 the Bessel function, k the wave number ($2*\pi / \lambda$), a the aperture radius, _ the variable and I_0 the incident intensity.
This simplification provides a good representation of the EEF. It has been demonstrated[9] that the spider diffraction has no major impact on the EEF. The experimental images (Figure 3) show an enhancement of the spider contribution with respect to the SCISIM images (Figure 2). To verify that this is not only due to diffraction, it is necessary to simulate as close as possible the diffraction pattern by calculating for each MS the Fresnel-Kirckkoff integral

$$I(x,y) = \left[\left| \frac{\sum_i \int_{ri}^{re} \int_{\alpha_i}^{\alpha_i+\pi/8} \rho \, e^{-ik\rho(x\cos(\theta)+y\sin(\theta))} d\theta \, d\rho}{\int_{ri}^{re} \int_0^{2\pi} \rho \, d\theta \, d\rho} \right| \right]^2 \qquad [4]$$

Where re and ri are the external and internal radii of the obstructed aperture, (x, y) the Cartesian image plane coordinates, _ and _ the polar coordinates in the entrance pupil plane and α_i the starting angle of a sector. Using [4] and [2], to add the images, the diffraction pattern of a complete MM is obtained as shown in figure 4. To save time, the diffraction pattern is calculated on _ of the focal plane image, and then rotated 4 times to reconstruct a complete image.

A second error source is the Wave Front Error (WFE) quality of the collimated beam. This one has been measured to 150 nm RMS. The Zernike coefficients of the interferometric alignment are used to simulate the impact of the collimator. Reconstructed WFE is given in figure 5.

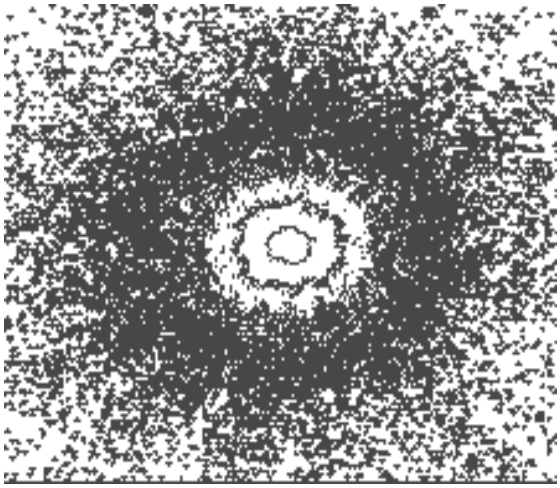

Figure 2 : **SCISIM simulated image of MM FM1 with XRB. Image on axis, sampled over 22.5 * 22.5 µm_ [logarithmic view]**

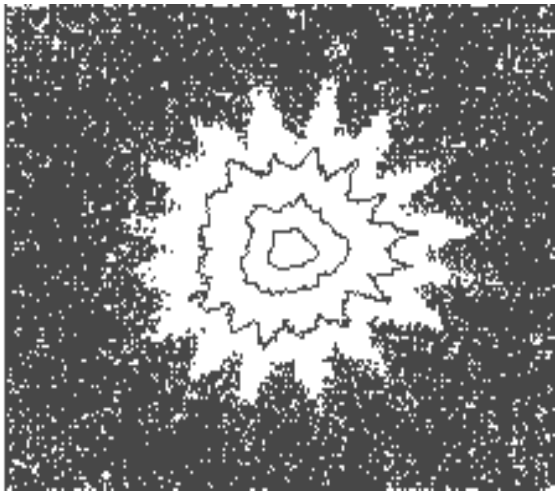

Figure 3 : **EUV experimental image of MM FM2 with XRB on axis [logarithmic view]**

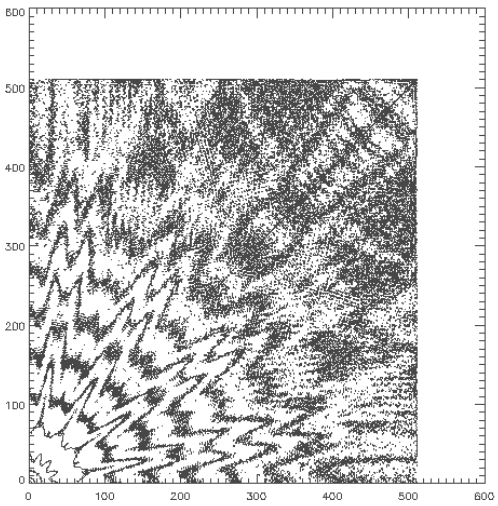

Figure 4 : **Diffraction pattern of a MM [logarithmic view]**

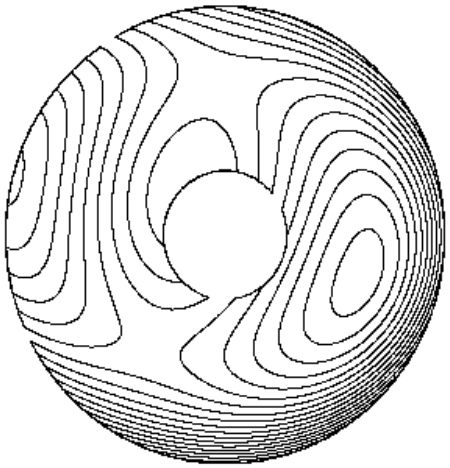

Figure 5 **: EUV collimator WFE reconstruction from the available Zernike coefficient**

5. ANALYSIS

Looking the figures 2 and 3, it appears that the simulated image does not fully render the observed image. However in terms of EEF and HEW, the two images are close to each other[5-8]. Other parameters to compare the "equivalence of the 2 images" are used. One is the correlation coefficient define as :

$$\rho = \frac{|\, FFT^{-1}(FFT(image1 - moy1).FFT^{*}(image2 - moy2))\,|}{\frac{1}{N?}\sqrt{\sum\sum |\, image1 - moy1\,|\,?\sum\sum |\, image2 - moy2\,|\,?}} \qquad [5]$$

the other is the $\chi\_$ defined as : $\chi? = \sum_{i=1}^{N}\sum_{j=1}^{N}\frac{1}{\sigma_{ij}^{2}}.(\exp erimental\ image_{ij} - simulated\ image_{ij})?$ [6]

The normalised $\chi\_$ (χ_norm), used hereafter, is the $\chi\_$ /N*N, with N*N the number of pixels. In the ideal case, the χ_norm and the correlation coefficient should be equal to 1 (or 100%). Applying these evaluation parameters to two successive experimental images show a χ_norm equal to 4, and a correlation factor equal to 99.99 %.

The simulated images are based on the single MS metrologies, and do not take into account the integration of the MS on the spiders and the integration of Mirror Interface Structure (MIS). This latter one interfaces the spider to the payload platform. These effects are present in the experimental image. The MIS integration generates this triangular shape of the PSF core. The MS to spider stress is observed in the amplification of the spider effect (16 spokes more apparent in the experimental measurement). The experimental images include also the instrument profile of the test set-up. The determination of the integration effect from the available data, is obtained from the following equation :

$$PSF_{expimage} = PSF_{SCISIM} \otimes PSF_{Diffracted} \otimes PSF_{WFECollimator} \otimes PSF_{MSintegration} \qquad [8]$$

To get the $PSF_{MSintegration}$ out of this relation, the SCISIM image (PSF_{SCISIM}) is convolved with the diffraction pattern ($PSF_{Diffracted}$) and with the collimator WFE PSF ($PSF_{WFECollimator}$). This convolution result is used to deconvolve the experimental image ($PSF_{exp\ image}$), so that only the last term (integration PSF) stays on the right in the equation 8. The most well-known deconvolution algorithms have been used : one is the Richardson-Lucy (RL) algorithm, the other is the Maximum Entropy (ME) principle. Both give similar results. However the RL method goes faster and gives better results for a same number of iterations. The evaluation of the impact of the diffraction and the collimator WFE shows that these are

negligible. The easiest and fastest method to improve the simulated model, is simply to deconvolve the experimental image by the simulated one. Once the integration PSF is available, this image is reconvolved with the simulated one. The results of this exercise are presented in the figures 6 and 7, for on-axis and off-axis (14 arcmin) images. 1000 deconvolution iterations are used. Table 1 presents the evaluation parameters of the simulation

FOV [arcmin]	EXP HEW	SCISIM HEW	reconvolved HEW	Correlation SCISIM [%]	Correlation reconvolved [%]	χ_ norm SCISIM	χ_ norm reconvolved
0	15.2	16.0	15.9	97.86	99.06	985	1056
7	15.2	15.1	16.1	97.61	99.05	657	954
14	18.9	20.0	19.9	96.19	98.51	211	228

Table 1. : Evaluation parameters of the model quality

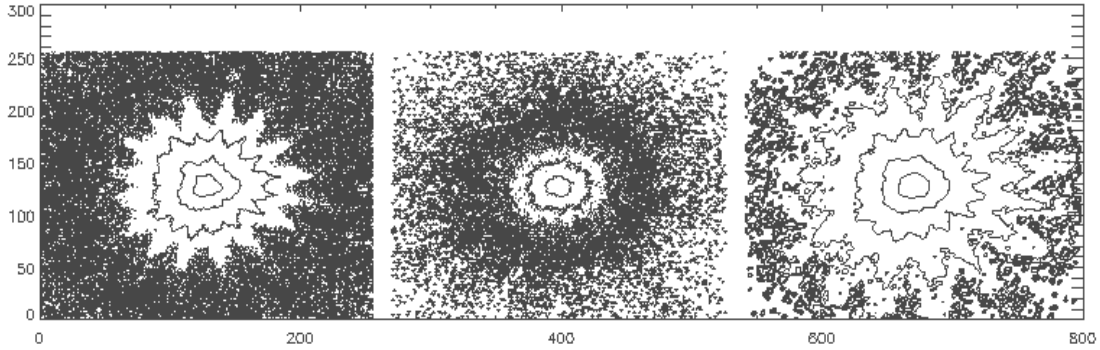

Figure 6 **: Comparison between on-axis experimental image (left), the SCISIM model (middle) and the reconvolved image (right) [logarithmic view]**

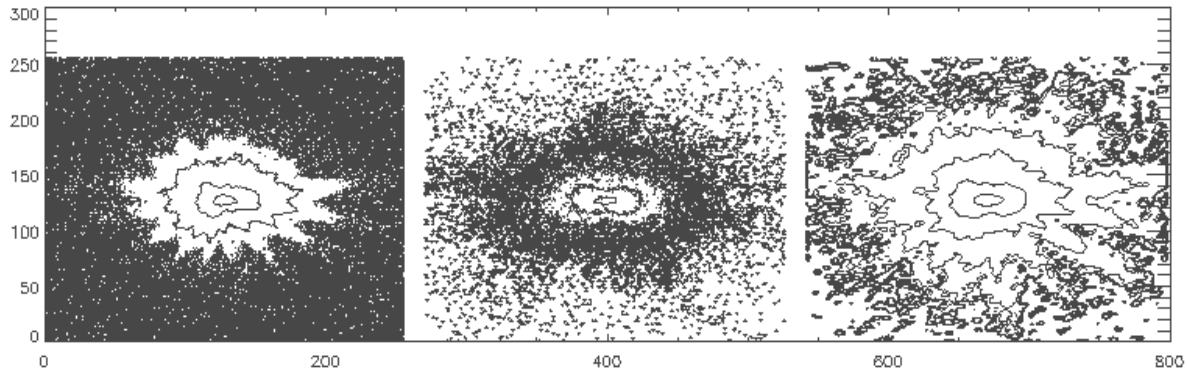

Figure 7 **: Comparison between off-axis (14 arcmin) experimental image (left), the SCISIM model (middle) and the reconvolved image (right) [logarithmic view]**

Using experimental data makes possible to improve the numerical model which is already close to reality, but misses mainly the integration effect. The numerical model is needed to generate the telescope calibration database. This one can now be improved by using the available integration contribution.
To save time and memory space linked to this method, parameterisation of the PSF will be performed. The method and results are given hereafter.

6. PSF PARAMETERISATION

The goal of the parameterisation, is to determine an analytical expression of the PSF in function of the elevation and azimuthal angle of the spot in the FOV.
A simple method is to fit the PSF by a 2D Gaussian profile. The fitting programme uses a conjugate gradient method. This provides already a good fitting (as good as SCISIM in terms of $\chi\_$) with respect to the experimental data, and needs only 8 parameters. To take into account the triangular shape, a second 2-D Gaussian is added with a triangular symmetry. Same is performed with a symmetry of 16 for the spider effects.

The analytical expression of the PSF is the following :

$$\begin{aligned} PSF(x,y) &= b_{13} + a_1.e^{-(b_1.(x-c_1)?+b_2.(y-c_2)?)}.(1+b_7.\cos(3.\theta+b_8)) \\ &+ a_2.e^{-(b_3.(x-c_3)?+b_4.(y-c_4)?)}.(1+b_9.\cos(3.\theta+b_{10})) \\ &+ a_3.e^{-(b_5.(x-c_5)?+b_6.(y-c_6)?)}.(1+b_{11}.\cos(16.\theta+b_{12})) \end{aligned} \quad [8]$$

All the parameters (a_i, b_i, c_i) are computed for all the available experimental FOV images. This allows to obtain expressions of the a_i, b_i, c_i versus FOV. Polynomes up to the second order are used .
After the gradient conjugate fitting, an optimisation in term of EEF is performed. This optimisation increases slightly the $\chi\_$ parameter but slightly reduces the correlation factor.
Results of the parameterisation in terms of image behaviour are presented in figure 8, in terms of EEF in figure 9, and in terms of image fitting parameter in the table hereafter.

FOV [arcmin]	EXP HEW	SCISIM HEW	Parameterised HEW	Correlation SCISIM [%]	Correlation parameterised [%]	X_ norm SCISIM	X_ norm parameterised
0	15.2”	16.0”	15.0”	97.86	99.47	985	127
7	15.2”	15.1”	17.1”	97.61	99.07	657	252
14	18.9”	20.0”	18.9”	96.19	98.96	211	52

Table 2 : Evaluation parameters of the analytical model

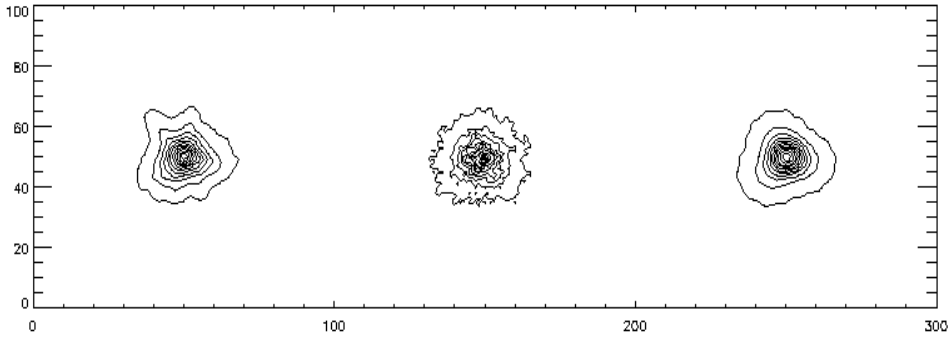

Figures 8 **: Comparison between experimental image (left), the SCISIM model (middle) and the parametrisation (right)**

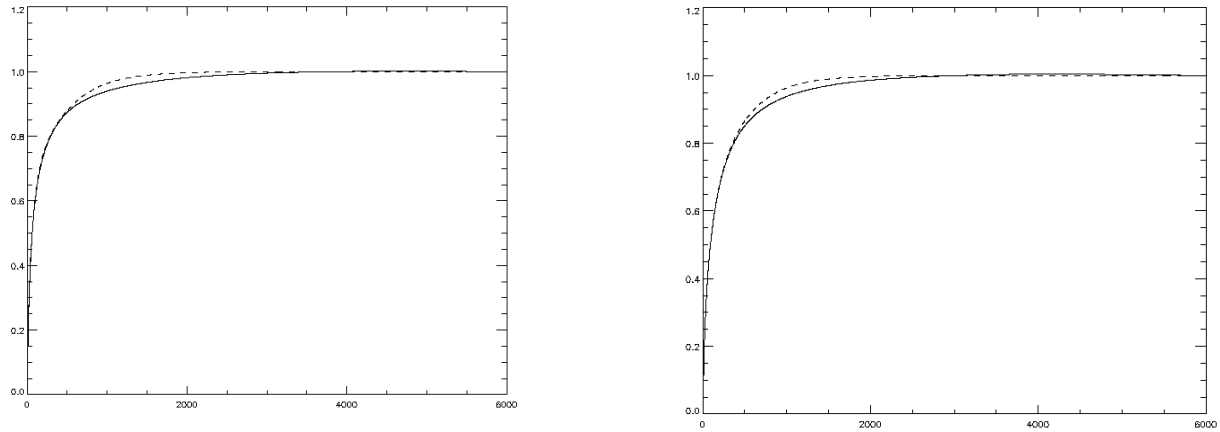

Figures 9: **Comparison between experimental image (solid lines) and parameterised (dotted lines) EEF on axis (left) and at + 14 arcmin in the FOV (right)**

7. PARAMETERISATION OF IN-ORBIT SIMULATED IMAGES

Fittings have been performed with experimental data of very good quality (low noise, good S/N ratio, high spatial resolution). The in-orbit images will have higher photon noise. The on board detectors have lower spatial resolutions. Two cases must be investigated : the EPIC MOS with a pixel size of 40×40 µm_ and the EPIC PN of 150×150 µm_ size. In-orbit images are simulated using ROSAT data. It is assumed that XMM has a throughput 4 times the one of ROSAT for EPIC MOS and 8 for EPIC PN. The observed ROSAT image has a count rate of $3.16\ 10^{-3}$ counts/s and a background level of $2.753\ 10^{-4}$ counts/s. A Poissonian noise is also added to the image to take into account the photon noise. The parameterisation is applied to these images.

For EPIC MOS the results are fairly good (HEW = 14.5 arcsec, 99.4 % as correlation factor and a normalised χ^2 of 128). For EPIC PN, the results are (HEW = 17.6 arcsec, 98.4 % as correlation factor and a normalised χ^2 of 447). In this case, the wings (the third Gaussian) are over-evaluated and the core is under evaluated. This information can be used to improve the parameterisation once in-orbit.

8. PROCESS VALIDATION ON SIMULATED IMAGES

8.1. Deconvolution methods comparison

For astronomical image restoration, deconvolution is also used. Magain, Courbin and Sohy[12] (MCS) have developed a new algorithm of deconvolution, which have better performance than the "classical" i.e. Richardson-Lucy (RL) and Maximum Entropy (ME) methods. It avoids the artefacts (rings around point source due to the violation of the Shannon theorem), and thus results in a good photometry. Moreover, it is independent of the offset, which is not the case of the RL and ME methods.

This method does not try to deconvolve by the entire PSF, but by a part of it, so that the deconvolved image respects the Shannon sampling theorem. Thus, the perfect image is not found (which is impossible to obtain because of sampling), but the image seen by a better instrument is obtained. This method supposes that the "perfect" image is composed of Dirac functions (the stars) and of backgrounds (the galaxies).

Three restorations of the same image (showed in figure 11) with the different algorithms has been made. The "perfect" image contains two sources of Gaussian shape, with a FWHM of 2 pixels, centred on (78.3, 78.5) and (183.8, 86.7) respectively, with an amplitude ratio of 2.25. The observed image is simply the convolution of this image by the EUV experimental image, with noise added. This image has been deconvolved with the different algorithms. The results can be seen on the figure 10 : MCS algorithm is indeed the best one, as predicted by theory.

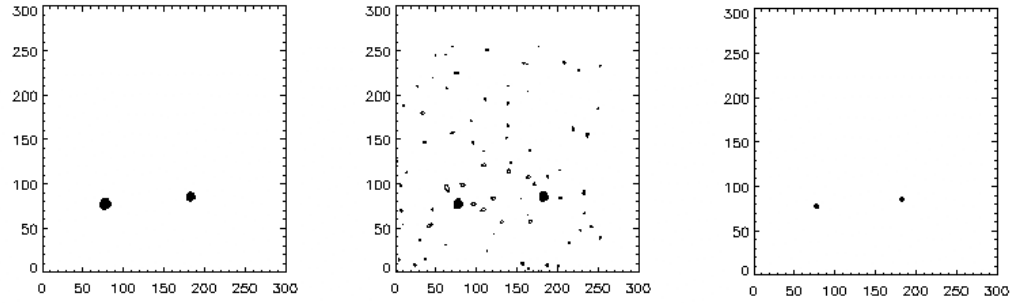

Figure 10: **Comparison between three deconvolution methods : Richardson-Lucy (left), Maximum Entropy (middle) and MCS (right).**

8.2. Image restoration with the different models

In order to compare the different models, we have simulated a noisy image and we have restored it by the three models (SCSIM numerical model, SCISIM convolved with deformation library images and parameterisation). The evaluation has been made on-axis and off-axis for the MM FM2 data. The smallest residua are found for the analytical models. Its also gives the best absolute results. All models present good performance for relative positions and amplitudes.

Model	$\chi_{\_}$ norm	Max. resi-duum	*star 1*			*star 2*			*Distance*		Amplitude ratio
			Centre		ampl.	centre		ampl.			
			x	y		x	y		x	y	
Perfect			78.3	78.5	1	183.8	86.7	0.444	105.5	8.2	2.25
SCISIM	1.009	2.347	79.95	79.16	1.35	185.48	87.37	0.508	105.53	8.21	2.66
SCISIM ⊗ $PSF_{integr.}$	0.986	1.633	78.30	78.64	1.56	183.75	86.80	0.613	105.45	8.16	2.54
Param	0.990	1.431	78.21	78.62	1.25	183.59	86.72	0.477	105.38	8.1	2.62

Table 3 : Comparison between the perfect image and the three deconvolution results, by each evoked model

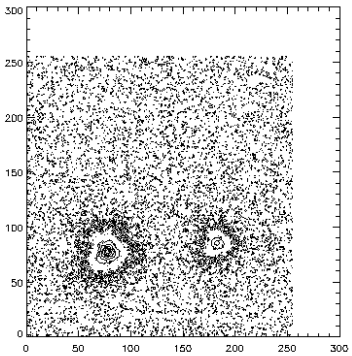

Figure 11: **Simulated on-axis image of 2 sources with noise**

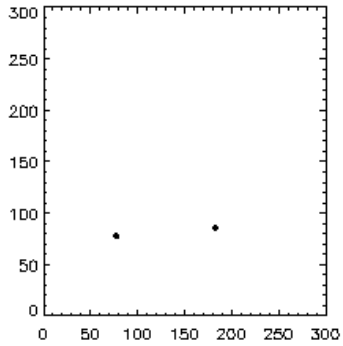

Figure 12 : **Result of the deconvolution with the analytical model**

8.3. Distortion calibration

Calibrations and parameterisations will be performed in-orbit. For example, MM distortion will be measured and calibrated. To do that, "shift pointing" method shall be used. Two images of the same star field, one on-axis and the other some arcmin off axis, are taken. To demonstrate the feasibility of the distortion calibration, "in-orbit" images (see paragraph 8) have been simulated, with a maximum distortion of 4 arcsec. Even on the raw images, the distortion can be evaluated, with an error of 17%. Once the image is restored by the MCS method, the expected distortion is found with an accuracy of 3%.

9. X-RAY CALIBRATION

These models can not be applied to energies higher than 2 keV because of the modification of the PSF shape. At energies higher that the gold M edge absorption the contribution of the large Mirror Shell decreases. These are mainly responsible of the non asymmetric appearance of the PSF. PANTER tests provide X-ray images, but these are not fully representative of the in-orbit images for many considerations exposed elsewhere[6]: these images are more axis-symmetrical than reality. An analytical model with no angular dependency may be applied. The PANTER images present scattering, one thing not existent on the FOCAL X EUV images. These images have been parameterised. To take scattering into account, a negative exponential is added, as it is shown hereafter :

$$PSF(x,y) = b_9 + a_1.e^{-(b_1.(x-c_1)?+b_2.(y-c_2)?)} + a_2.e^{-(b_3.(x-c_3)?+b_4.(y-c_4)?)} + a_3.e^{-(b_5.(x-c_5)?+b_6.(y-c_6)?)} + a_4.e^{-(b_7.|x-c_7|+b_8.|y-c_8|)}$$

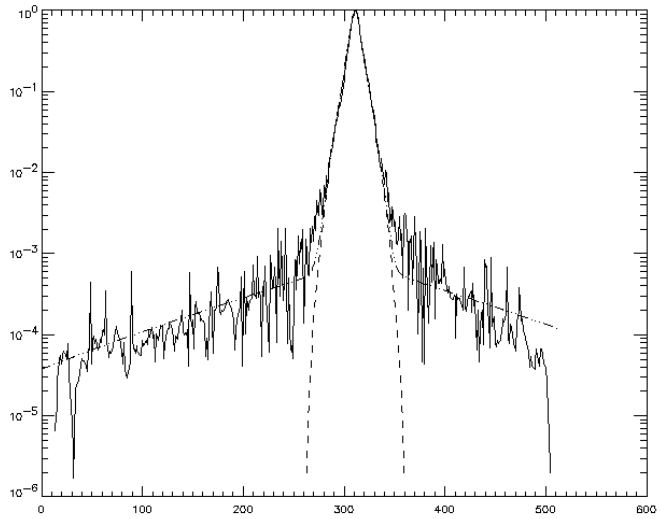

Figure 13 : **Comparison between on-axis experimental image (solid line) at 8 keV, three Gaussian parameterisation (dashed line) and two Gaussian + one negative exponential (dash-dot line) .**

10. CONCLUSIONS

Three models have been compared in this paper :

- SCISIM model, developed by ESTEC and based on MS metrology
- Library model, where integration impacts are memorised
- Analytical model

The SCISIM model gives a good representation of the MM PSF. However, it does not restore the angular asymmetry of the experimental images. This effect is not integrated by construction of the model itself, in which only the metrological data before MS integration are used. It has been demonstrated by simulation that this triangular behaviour in

the PSF comes from Mirror Interface Structure (MIS) on the spider. This stress is not included in the SCISIM model. To evaluate this effect, and include it in a model, the diffraction of the MM and collimator WFE contribution were calculated. These are negligible, so that the deconvolution between SCIM images and experimental images gives straightforward the impact contribution of the MIS integration on the PSF images. All those impacts are memorised in a library for a sampled number of images in the FOV. Another solution, saving computer time and memory space, is also developed. A simple analytical model, easy to compute, is found. Good fitting is achieved using only three 2D Gaussian functions combined with a cos (3.θ) for the triangular shape and a cos (16.θ) for the spider enhancement contribution. All the developed models give good results, but the analytical one presents the best performances, including in restoration problems: even distortion can be precisely calibrated. The parameterisation method has been developed with on-ground images. They can be applied for energies lower than 2 keV, with very good accuracy. The method can be extrapolated to all the energies, integrating other function such as a negative exponential to modelise scattering.

Acknowledgements

The authors are grateful to all CSL staff who worked days and nights to provide all these useful and high quality data to perform this work.
The vertical facility at CSL was funded by ESA XMM project under the contract number 9939/92/NL/PP.
The XMM FM MM mirrors were replicated and integrated by MEDIA LARIO under ESA contract number 0545/93/NL/RE.
Many thanks go to the Magin, Sohy and Courbin team, who gives us a lot of advises in the image restoration field, and allows the use of their softwares.

References

1. D. Lumb, H. Eggel, R. Lainé, A Peacock, “X-ray Multi-Mirror Mission – an overview”, SPIE 2808-32, Denver 1996.
2. J. Ph. Tock, J-P. Collette, Y. Stockman, “Calibration and upgrades of the XMM vertical EUV/X test facility: FOCALX”, SPIE 3114, pg 554, San Diego 1997.
3. Y. Stockman, I. Domken, H. Hansen, J.Ph. Tock, D. de Chambure, Ph. Gondoin, “XMM Flight Mirror Modules environmental and optical testing”, SPIE 3444, pg 302-312, San Diego 1998
4. Y. Stockman, I. Domken, H. Hansen, J.Ph. Tock, T.A. Decker, A. Rasmussen, T. den Boggende, J.W. den Herder, G. Bagnasco, D. de Chambure, C. Erd, Ph. Gondoin, “XMM Flight Mirror Module with Reflection Grating Assembly and X-ray baffle testing”, SPIE 3445 , San Diego 1998.
5. Ph. Gondoin, B. Aschenbach, M. Deijeysbergen, R. Egger, F. Jansen, Y. Stockman, J.P.Tock, “Calibration of the first XMM Flight Mirror Module I – Image quality”, SPIE 3444, pg 280, San Diego 1998.
6. Ph. Gondoin, B. Aschenbach, M. Deijeysbergen, R. Egger, F. Jansen, Y. Stockman, J.P.Tock, “Calibration of the first XMM Flight Mirror Module II – Effective area”, SPIE 3444, pg 290, San Diego 1998.
7. Y. Stockman, P. Barzin, H. Hansen, JP. Tock, “XMM Flight Mirror Module testing and Manufacturing”, Conference SPIE 3766, Denver 1999.
8. Ph. Gondoin, M. Deijeysbergen, K. van Katwijk, D. Lumb, A.J. Peacock, “Simulation of the XMM performance based on metrology data”, SPIE 2808, pg 379-388, Denver, 1996
9. P. Conconi, U. Bergamini, O. Citterio, G. Grimi, M. Ghigo, F. Mazzoleni, “Evaluation by UV-optical measurements of the imaging quality of grazing incidence x-ray optics”, SPIE 2011, pg 89-99 San Diego 1993.
10. H.F.A. Tschunko, “Imaging performance of annular apertures”, Applied Optics, vol 13 n8, pg 1820, 1974
11. Born and Wolf, “Principle of Optics”, 6th edition, Pergamon, 1990
12. P.Magain, C.Courbin, S.Sohy, “Deconvolution with correct sampling”, ApJ 494, pg 472-477, 1998